

Journal of Medical Imaging

MedicalImaging.SPIEDigitalLibrary.org

Quantitative identification of magnetic resonance imaging features of prostate cancer response following laser ablation and radical prostatectomy

Geert J. S. Litjens
Henkjan J. Huisman
Robin M. Elliott
Natalie Nc. Shih
Michael D. Feldman
Satish Viswanath
Jurgen J. Fütterer
Joyce G. R. Bomers
Anant Madabhushi

Quantitative identification of magnetic resonance imaging features of prostate cancer response following laser ablation and radical prostatectomy

Geert J. S. Litjens,^{a,*} Henkjan J. Huisman,^a Robin M. Elliott,^b Natalie Nc. Shih,^c Michael D. Feldman,^c Satish Viswanath,^b Jurgen J. Fütterer,^{a,d} Joyce G. R. Bomers,^a and Anant Madabhushi^b

^aRadboud University Medical Center, Department of Radiology, Nijmegen 6525GA, The Netherlands

^bCase Western Reserve University, Department of Biomedical Engineering, Cleveland, Ohio 44106, United States

^cUniversity of Pennsylvania, Department of Pathology and Laboratory Medicine, Philadelphia, Pennsylvania 19104, United States

^dUniversity of Twente, Institute for Biomedical Technology and Technical Medicine, Enschede 7522NB, The Netherlands

Abstract. Laser interstitial thermotherapy (LITT) is a relatively new focal therapy technique for the ablation of localized prostate cancer. In this study, for the first time, we are integrating *ex vivo* pathology and magnetic resonance imaging (MRI) to assess the imaging characteristics of prostate cancer and treatment changes following LITT. Via a unique clinical trial, which gave us the availability of *ex vivo* histology and pre- and post-LITT MRIs, (1) we investigated the imaging characteristics of treatment effects and residual disease, and (2) evaluated treatment-induced feature changes in the ablated area relative to the residual disease. First, a pathologist annotated the ablated area and the residual disease on the *ex vivo* histology. Subsequently, we transferred the annotations to the post-LITT MRI using a semi-automatic elastic registration. The pre- and post-LITT MRIs were registered and features were extracted. A scoring metric based on the change in median pre- and post-LITT feature values was introduced, which allowed us to identify the most treatment responsive features. Our results show that (1) image characteristics for treatment effects and residual disease are different, and (2) the change of feature values between pre- and post-LITT MRIs can be a quantitative biomarker for treatment response. Finally, using feature change improved discrimination between the residual disease and treatment effects. © 2014 Society of Photo-Optical Instrumentation Engineers (SPIE) [DOI: 10.1117/1.JMI.1.3.035001]

Keywords: laser ablation therapy; prostate cancer; magnetic resonance imaging; treatment response.

Paper 14035PR received Mar. 31, 2014; revised manuscript received Aug. 13, 2014; accepted for publication Sep. 23, 2014; published online Oct. 27, 2014.

1 Introduction

Radical treatment of prostate cancer is known for its relatively high incidence of side-effects such as incontinence and impotence.¹ Furthermore, most prostate cancer is not aggressive and might not warrant radical therapy. This has spurred substantial interest in less radical, localized therapy options. Examples are cryo-ablation, high-intensity focused ultrasound, or laser-ablation therapy.^{2,3} Laser interstitial thermotherapy (LITT) is one such focal therapeutic procedure, which is compatible with magnetic resonance imaging (MRI), allowing for high resolution *in vivo* imaging to be used in LITT procedures for treatment guidance to the index lesion.⁴ Furthermore, from previous studies on LITT for liver lesions, we know that the extent of tissue necrosis post-LITT is visible on MRI.⁵ However, there is very little work describing the imaging characteristics of LITT-induced changes in the prostate.⁶

Understanding changes in MRI features post-LITT is important for accurate follow-up of the patient, because it will allow the clinician to assess whether the ablation was successful (i.e., whether all the primary tumor has disappeared). If residual disease is present, the area could be re-ablated or a different therapy option could be chosen. Furthermore, quantitative observations of LITT-related changes on prostate MRI could address how to identify the benign LITT-related changes (e.g., edema and

necrosis) that can mask the presence of residual cancer. This implies a need for co-registration and image analysis methods to quantitatively compare pre- and post-LITT MRIs in order to identify the changes in MRI parameters that can describe LITT-related changes within the prostate.

Treatment evaluation of therapeutic options for prostate cancer has primarily been examined for radiation treatment in a number of qualitative studies.^{7,8} For LITT, a phase I trial found good correlation between volumes of thermal damage that were visible on MRI and those determined via staining of *ex vivo* surgical prostatectomy specimens from the patients who had previously undergone LITT.⁹ Additionally, while the ablated volume measured on MRI was marginally overestimated compared to pathology, MR images demonstrated excellent capability in discriminating nonviable necrotic tissue and postablation.

However, for imaging changes between pre- and post-LITT MRIs, only Viswanath et al. investigated the imaging characteristics of LITT-related changes on MRI⁶ following treatment for prostate cancer. While they found changes in imaging markers following LITT and specifically found that there were particular imaging markers that revealed more dramatic changes compared to other markers, all the analysis was limited to the ablation zone. Since no histopathology was available, it was not possible to rigorously evaluate whether the changes in imaging markers

*Address all correspondence to: Geert J. S. Litjens, E-mail: geert.litjens@radboudumc.nl

were driven by treatment effects or by residual disease. Additionally, the lack of histopathology meant that it was not possible to evaluate whether the residual disease had itself undergone any imaging changes and whether these changes were discernible on MRI.

The aim of this study was to perform a preliminary quantitative assessment of the imaging characteristics of prostate cancer and benign confounding treatment changes following LITT on 3 T multiparametric MRIs. A clinical trial at the Radboud University Medical Center, in which four patients underwent a prostatectomy after LITT treatment, yielded *ex vivo* histopathologic specimens along with pre- and post-LITT MRIs. Using these data, (1) we identified the computer extracted MRI signatures associated with treatment effects and residual disease following LITT on MRI, and (2) subsequently evaluated the previously identified imaging signatures in distinguishing LITT-induced changes in the ablated area from those in the residual disease on MRI. A flowchart detailing the pipeline and methodology is shown in Fig. 1.

To investigate (1), we first need to identify treatment effects and residual disease on histology, and subsequently establish a spatial correspondence between the post-LITT MRI and the histology. Establishing spatial correspondence means that we map the extent of residual disease and ablated tissue from histopathology to MRI as accurately as possible. This is of course inherently limited by the lowest resolution unit in both modalities, which is an MRI voxel (approximately 0.5 mm in T2-weighted MRI). To this end, first the histology was annotated by a pathologist, after which we performed a careful semi-automatic elastic registration of the histology to the post-LITT MRI.¹⁰ Finally, the histology annotations were propagated to the post-LITT MRI and computer extracted features were obtained (Table 1).

The multiparametric prostate MRIs (both pre- and post-LITT) in this study consisted of the typical T2-weighted, diffusion weighted, and dynamic contrast-enhanced (DCE) imaging.^{15,16} From clinical guidelines, we know that the T2-weighted images are especially useful for assessing the texture

of prostate lesions.¹⁶ Prostate cancer in the transition zone exhibits a so-called “erased charcoal sign,” a smudge-like dark texture on T2-weighted images¹⁶ and previous work has suggested that ablated areas have a different textured appearance compared to normal or benign tissue.⁶

Diffusion-weighted imaging is specifically useful for characterizing the microscopic tissue structure, enabling us to assess traits-like cell density at the MRI level. Prostate cancer has a high cellular density compared to the normal glandular structure of the prostate. This results in a reduced diffusivity in cancerous tissue, and thus a high signal in high *b*-value images and subsequently lower apparent diffusion coefficient values. LITT tends to cause necrosis and formation of scar tissue and might alter diffusivity in the tissue. Furthermore, prostate cancer lesions tend to have a focal appearance on diffusion-weighted imaging, the shape of which might change due to therapy.

Prostate cancer lesions tend to have leaky microvasculature, which results in fast initial enhancement and wash-out of contrast agent in DCE MRI. Additionally, inflammation and tissue death (necrosis/apoptosis) caused by the treatment might cause blood flow and vascular changes in the ablated area.

To extract the changes of feature values between pre- and post-LITT to assess their potential in discriminating successfully ablated tissue from residual disease (2), we first need to register the pre- and post-LITT MRIs to establish spatial correspondence. We then extracted the same computer derived image features for the pre-LITT MRI as for the post-LITT MRI (Table 1). Subsequently, a feature score is calculated to identify the features which changed most in the treatment area relative to the residual disease (from pre- to post-LITT MRIs). After identifying the features that reveal the largest differential change between the residual cancer and benign thermally changed regions, a fuzzy C-means clustering algorithm is used to evaluate their performance.

The structure of this paper is as follows: Sec. 2 will describe the data and the experimental design. In Sec. 3 we will assess and discuss the results of our experiments. Finally, in Sec. 4 we

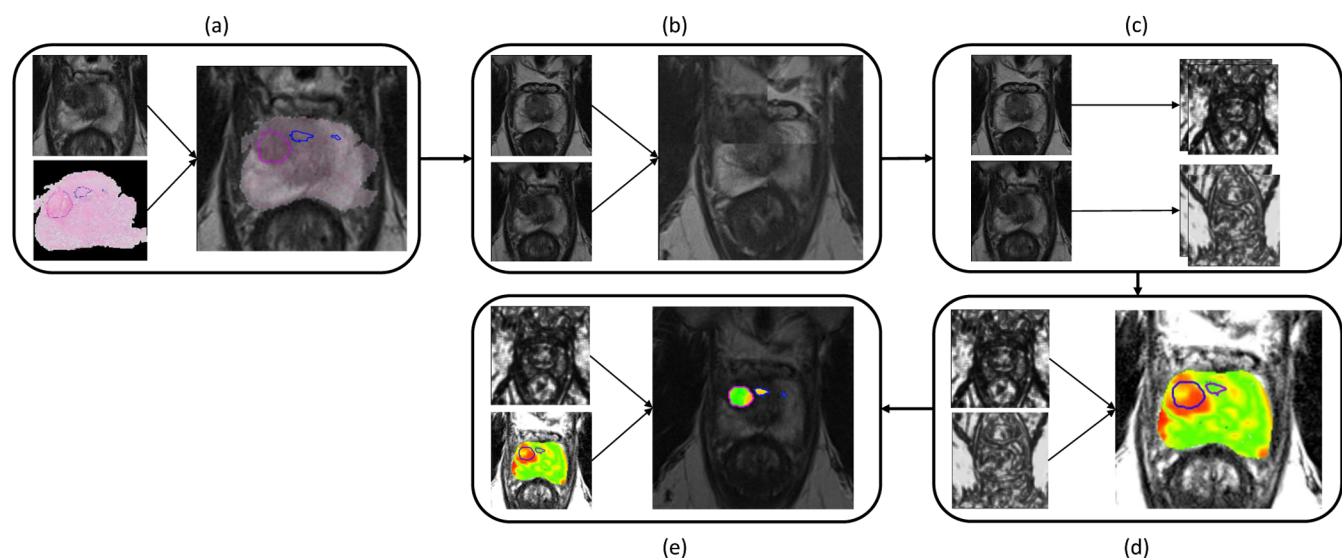


Fig. 1 Flowchart detailing the process of (a) co-registration of histopathology and MRI using a semi-automated thin plate spline approach, (b) registration of pre- and post-LITT MRIs using affine registration with localized mutual information, (c) extraction of features (Table 1) and (d) calculation of relative feature change and finally (e) the clustering result to detect residual disease using fuzzy C-means clustering.

Table 1 Summary of features and feature settings calculated for both the pre- and post-LITT MRIs.

Category	Feature name	MR parameter	Feature settings
Intensity	(Pseudo)T2-map ¹¹	T2W	
	ADC	DWI	
	b800	DWI	
Texture	2-D multiscale Gaussian derivatives ¹¹	T2Map	Up to second order, $\sigma = 2.0, 2.67, 4.1$ and 6.0 mm
	2-D Haralick texture measures ¹²	T2Map	Kernel sizes 3, 5, 7 voxels
	2-D multiangle Gabor ¹²	T2Map	Four angles: $0, \pi/4, \pi/2, 3\pi/4$, $\lambda = 1.5, 2$, and 4 voxels
	2-D Li multiscale blobness ¹³	T2Map, ADC, b800, Ktrans, Kep, Ve, time-to-peak, maximum enhancement, wash-out rate	$\sigma = 2.0, 2.67, 4.1$, and 6
Pharmacokinetic	Curve fitting parameters ¹⁴	Dynamic contrast-enhanced (DCE)	Time to peak, maximum enhancement, wash-out rate
	Std. Tofts PK model ¹⁴	DCE	Ktrans, Kep, Ve

will come back to the initial hypothesis and offer some concluding remarks.

2 Experimental Design

2.1 Data Description

Four patients underwent both pre- and post-LITT multiparametric MRIs (3 T, Siemens Skyra MR scanner, Siemens, Erlangen, Germany). All studies were acquired with only a pelvic phased-array coil, except the post-LITT MRI study of one patient, which was acquired with an endorectal coil. After the post-LITT MRI, all patients underwent a radical prostatectomy. Specimens were cut perpendicular to the dorsal-rectal surface to make sure MRI slices and prostatectomy slices were parallel. Subsequently, the slide with the largest ablated area was digitized using an Olympus digital slide scanner at 20 \times . An experienced pathologist annotated areas of LITT-induced changes and residual disease on the prostatectomy slide including the largest ablated area. One patient was subsequently excluded because no residual disease was present. Both the pre- and post-LITT MRIs consisted of T2-weighted imaging, a diffusion-weighted sequence including three b -values (50, 400, and 800), a DCE time series (36 time points, 4 s temporal resolution), and a proton density-weighted image. The scanner software calculated an apparent diffusion coefficient (ADC) based on the diffusion-weighted imaging.

2.2 Histology/Magnetic Resonance Imaging Registration

The pathology annotations were transferred to the post-LITT MRI by establishing slice correspondences, and subsequently registering the whole-mount slide to the post-LITT MRI by using a thin plate spline registration technique.¹² First, slice

correspondence was established by identifying the relative corresponding slice via:

$$S_{MR} = \frac{T_{MR}}{T_P} S_P, \quad (1)$$

where S_{MR} is the slice number in the MRI, T_{MR} is the total number of slices in the MRI the prostate is visible on, T_P is the total number of prostatectomy slices, and S_P is the prostatectomy slice number which was digitized. Subsequently, an image analysis researcher and a radiologist looked at the identified MRI slice and the adjacent slices and picked the slice with the best visual match. During this process, they were blinded to the histopathology annotations.

The process, in a step-by-step fashion, is as follows:

1. A pathologist annotated the areas of residual disease and successfully ablated tissue on the whole-mount prostatectomy slide using a contouring tool.
2. The slice in the MRI, which corresponds to the prostatectomy slide, was established by an image analysis researcher under the supervision of a radiologist by comparing landmarks in pathology and MRI.
3. Corresponding points were indicated on the prostate boundary for both the prostatectomy slide and the MRI slice (Fig. 2).
4. A thin plate spline transformation was calculated to move from the prostatectomy coordinate space to MRI coordinate space.¹⁷
5. The histopathology image was transformed into the MRI space using this thin plate spline transformation

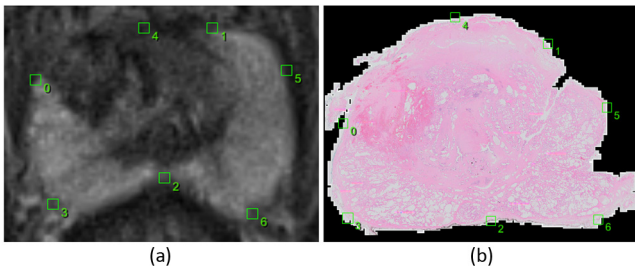


Fig. 2 Example images of the corresponding points selected by the observer in the post-LITT axial T2-weighted MRI (a) and the corresponding histopathology slice (b). Points 0 and 1 indicate the ends of the peripheral zone, point 2 is the thinnest point of the peripheral zone, points 3 and 6 are the thickest parts and point 4 is the top part of the prostate when drawing a line from point 2 through the urethra to the top of the prostate. Point 5 was added due to the tear in the tissue.

and a visual assessment of registration quality was made.

6. The annotations of the pathologist were subsequently morphed to the MRI using the same transformation.
7. The pre-LITT MRI was subsequently registered (affine/elastic) to the post-LITT MRI to establish spatial correspondence [Figs. 1(b) and 4].

An example of the results from this process is shown in Figs. 3 and 4.

2.3 Pre-LITT/Post-LITT Magnetic Resonance Imaging Registration

To establish spatial correspondence between the post- and pre-LITT MRIs, we used the elastix registration software.¹⁸ For two

out of three patients we applied an affine registration, for one patient we applied an elastic registration because the pre-LITT MRI was acquired with an endorectal coil, whereas the post-LITT MRI was acquired with only a pelvic phased-array coil. Registration was performed in two steps, first a translation component was estimated after which either the affine transformation matrix or the *b*-spline elastic transformation grid was determined. Localized mutual information was used as a similarity metric to drive the registrations. An example of the result is shown in Fig. 4.

2.4 Feature Calculation and Scoring

In total, 93 features were extracted to establish the imaging characteristics of benign confounding treatment changes and residual disease. An overview of all features used in this study is given in Table 1.

2.4.1 Intensity standardization

Intensity drift is an issue that is well known in MRI.¹² This means that intensities differ from scanner to scanner and even from protocol to protocol or scan to scan on the same scanner. Intensity drift might also have happened between the pre- and post-LITT images. To circumvent this issue in T2-weighted images, we can calculate a (pseudo)T2-map using the transverse T2W-image and the proton density-weighted image as described in Ref. 19. This approach uses MR signal equations and a muscle reference region of interest to reduce the intensity drift between the pre- and post-LITT acquisitions.

2.4.2 T2-weighted imaging features

For the T2-weighted image, we calculated several texture features. From previous studies, we know that there exists a

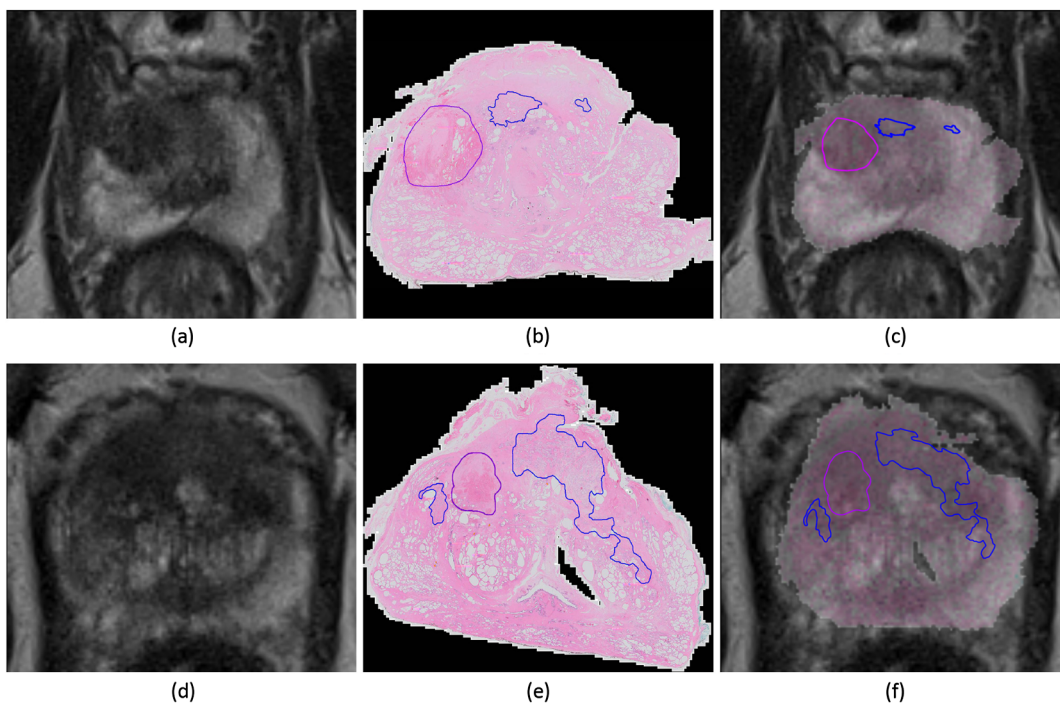


Fig. 3 Example images of the post-LITT MRI (a and d) and H and E stained prostatectomy slides (b and e) and the result of the subsequent MRI/histology registration (c and f). Ablated area in purple, residual disease in blue.

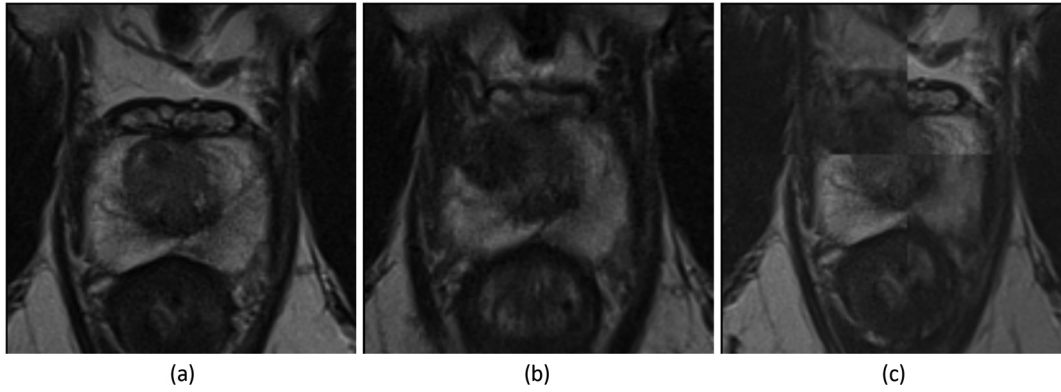


Fig. 4 Example images of the pre-LITT axial T2-weighted MRI (a), post-LITT MRI (b), and the subsequent affine registration result in a checkerboard form (c). Registration was performed using localized mutual information as a metric.

difference in texture between normal prostate tissue and LITT therapy effects.⁶ Furthermore, there are distinct texture differences between prostate cancer and normal prostate tissue.¹⁶ We hypothesize that there also must exist a texture difference between residual prostate cancer and benign LITT-related changes. We used 13 Haralick texture features using three kernel sizes (3, 5, and 7 voxels), Gabor texture features using four different angles and three different wavelengths between 1 and 6 mm and Gaussian derivatives up to the second order using four different scales between 1 and 6 mm.¹² The texture features were all calculated on the (pseudo)T2-map. One of the advantages of kernel-based features is that they are not dependent on single voxel values and take neighborhood information into account. This makes them more robust to small registration inaccuracies.

2.4.3 Diffusion-weighted imaging features

For the diffusion-weighted imaging, we directly used the ADC values and the b800 image intensities. To take advantage of the fact that prostate lesions tend to exhibit a focal appearance on diffusion-weighted imaging and that treatment effects may not show this feature, we implemented the multiscale blobness filter proposed by Li et al.²⁰ and calculated the filter using four scales between 1 and 6 mm on the b800 and ADC images.

2.4.4 Dynamic contrast-enhanced imaging features

DCE MRI also tends to suffer from scanner and protocol dependency. To remove this dependency and extract the most useful information from these curves, we implemented curve fitting and pharmacokinetic modeling routines as presented in Refs. 14, 21, and 22. The curve fitting routine uses a two-exponential curve model and was implemented to enable faster and more robust pharmacokinetic modeling. The pharmacokinetic model that was implemented was the standard Tofts model, which neglects the vascular component in each voxel. The temporal resolution of the DCE time series was 4 s. To capture characteristics on the microvasculature, we included a total of three curve features (time to peak, washout rate, and maximum enhancement)²² and three pharmacokinetic features (K_{trans} , K^{ep} , V_e).¹⁴ The microvasculature might be affected due to local tissue death and inflammation effects in the ablated area, as has been observed in the ablation of liver lesions.²

Furthermore, as cancer also tends to have a focal appearance on DCE MRI,¹⁶ we also calculate the Li blobness filter on the K_{trans} , K^{ep} , V_e , maximum enhancement, time-to-peak and wash-out rate images.

2.4.5 Feature scoring

Feature values may change both in the successfully ablated area and in the residual disease area. As such, a feature which shows a large change in one area and little in the other is most discriminative. We try to quantify this using a feature score. For each feature, a score was established by calculating the voxel differences between the pre- and post-LITT MRIs in both the ablated and residual disease regions. A relative change per feature was calculated using:

$$d_r(f) = \text{median}_{c \in V} \left(\frac{f_{\text{post}}(c) - f_{\text{pre}}(c)}{f_{\text{pre}}(c)} \right), \quad (2)$$

$$S(f) = ||d_r(f)|_{\text{Res}} - |d_r(f)|_{\text{Abl}}|, \quad (3)$$

where d_r is the relative change for feature f . V is the set of all voxels in a region and c is a voxel. f_{post} and f_{pre} are the features f on the post- and pre-LITT MRIs, respectively. The score in Eq. 2 is then defined as the absolute difference between the relative change in the ablated area $d_p(f)_{\text{Abl}}$ and in the residual disease $d_p(f)_{\text{Res}}$. This definition allows us to find features that are important in differentiating between residual disease and therapy effects. The median score over all patients was obtained as the overall score for that feature. Examples of the features' changes are shown in Fig. 5.

2.5 Clustering Approach to Discriminate Residual Disease from Successfully Ablated Tissue

A fuzzy C-means clustering to separate residual disease and treatment effects was performed for each patient. Clustering was chosen due to the limited amount of data (three patients) we have in this study. A supervised classification approach typically tends to perform better than unsupervised methods like clustering, however, only when enough training data are available to accurately train the classifier. Fuzzy C-means was chosen because it results in a likelihood of belonging to a cluster instead of a hard classification, which in turn allows us to evaluate the

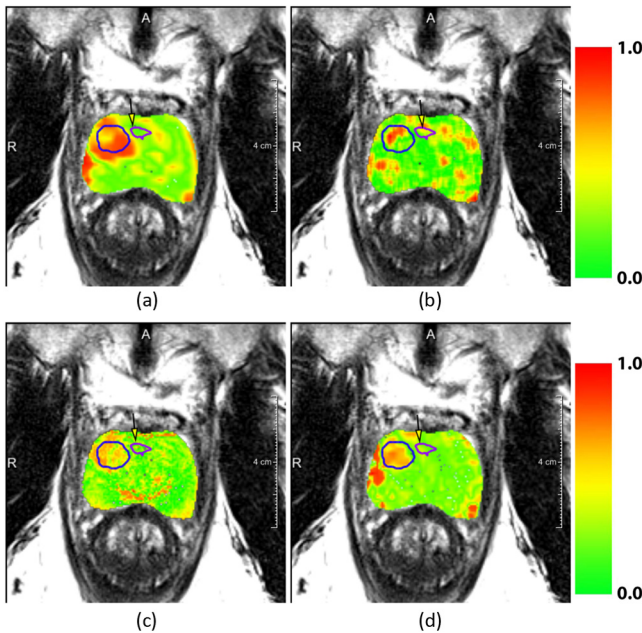


Fig. 5 Overlays of normalized feature change between pre- and post-treatment MRIs. Figures (a), (b), (c), and (d) represent the features K^{ep} , Haralick correlation, (Pseudo)T2-Map, and V_e respectively. In the overlay, red indicates areas of high relative change and green of low relative change. The successfully ablated area is indicated in a blue contour and the purple contour indicates residual disease. The residual disease area is also indicated with a yellow arrow.

results using receiver-operating characteristic (ROC) analysis. The input to the clustering algorithm is unlabeled voxel feature data from the region encompassing both the ablated area and the residual disease. We repeat the clustering 100 times with different initial cluster means to obtain the result with a minimal root-mean-squared error. We perform the experiment with only the computer extracted feature, and subsequently repeat the experiment, with the addition of feature change of the top 10 scoring features as extra features.

3 Experimental Results and Discussions

Our objectives were to identify features which (1) allow discrimination between residual disease and treatment effects and (2) showed the most treatment-related change relative to the residual disease. Finally, we wanted to incorporate this information to (3) improve detection of residual disease.

3.1 Objective 1: What are the Imaging Characteristics Specific for Residual Disease and Treatment Effects?

For objective (1), we show in Table 3, column 1 that our computer extracted features are able to identify residual disease with an area under the ROC curve (AUC) up to 0.80. However, it can also be seen that this differs from patient to patient. This indicates that the differences between residual disease and successfully ablated area imaging characteristics cannot fully be explained by the appearance on the post-LITT MRI.

3.2 Objective 2: Identify Features that Show Discriminative Change in Successfully Ablated Tissue Relative to Residual Disease

For objective (2), we present the 10 features with the highest feature change between pre- and post-LITT MRIs in Table 2 and Fig. 6. One can appreciate that the DCE MRI (positions 1, 5, and 10 in Table 2) and the T2-weighted texture features (positions 2, 3, 4, 6, 7, 8, and 9 in Table 2) especially show large differences between pre- and post-LITT MRIs. We hypothesize that due to scar tissue formation in the ablated area, the texture changes substantially because most of the scar tissue will be connective tissue, with few live cells. Compared to the residual disease, which will still have a lot of viable cancer cells, it is likely to result in distinct textures. Furthermore, blood flow and vascular content will probably be markedly reduced in scar tissue. If we look at Table 2, we can see that the contrast agent transfer constant K_{ep} is markedly reduced in the successfully ablated area, indicating reduced blood flow. Furthermore, the time to peak has been substantially increased, while it has decreased in the residual disease. The reason time to peak reduces in residual disease might be due to inflammation effects or the cancer needing more nutrients to recover from the effects of the treatment. As scar tissue also has very limited diffusivity (similar to prostate cancer lesions), the diffusion-weighted imaging might be less useful to assess treatment response, even though it is a very important modality for the initial diagnosis of prostate cancer.

Table 2 The 10 top scoring features. Columns 3 and 4 show the normalized relative changes Eq. (1) in feature value between the pre- and post-LITT MRIs for both residual disease and treated area. It can be seen that all selected features are related to either T2W or DCE MRI. Furthermore, texture features show larger changes in both residual disease and successfully ablated tissue; however, the relative change is similar to the pharmacokinetic features.

Rank	Feature	Median normalized relative change in		
		Residual disease	Treated area	MRI parameter
1	K_{ep}	0.05	-0.11	DCE
2	Gabor $\theta = 0, \lambda = 1.5$	0.07	0.14	T2W
3	Gaussian derivative— $\sigma = 2.0$	0.08	0.17	T2W
4	T2Map	0.07	0.12	T2W
5	K_{trans}	0.09	0.15	DCE
6	Gaussian derivative— $\sigma = 2.8$	0.09	0.14	T2W
7	Haralick correlation (ws = 7)	0.26	-0.40	T2W
8	Gabor $\theta = 0.39, \lambda = 1.5$	0.09	0.14	T2W
9	Gaussian derivative X $\sigma = 6.0$	0.37	0.54	T2W
10	Time to peak	-0.05	0.07	DCE

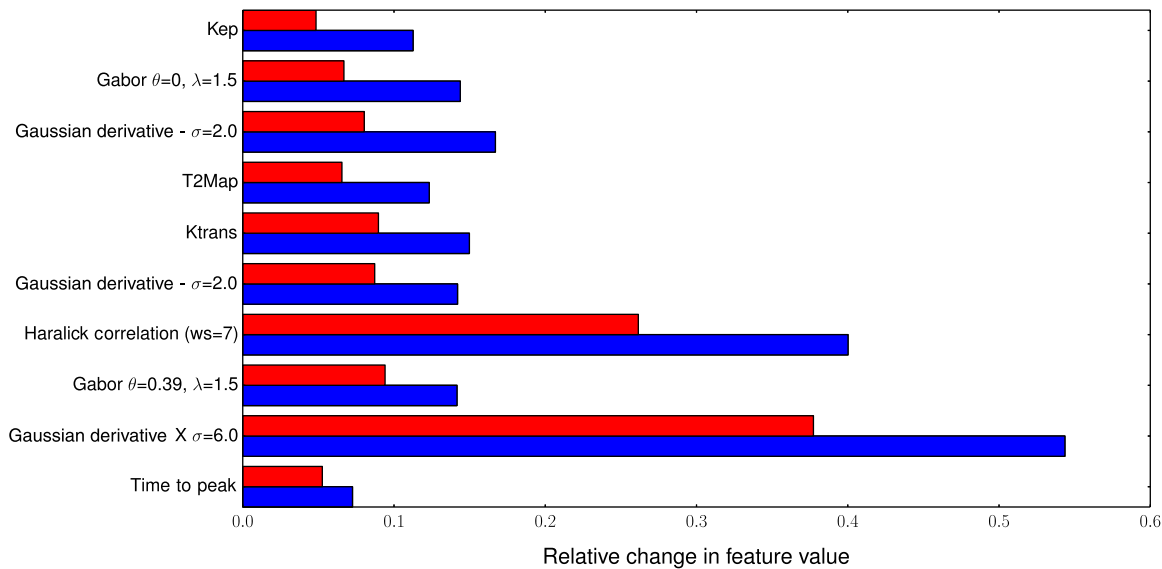


Fig. 6 Relative change in feature value between residual disease (red, top bars) and the successfully ablated area (blue, bottom bars) for the top 10 scoring features (top to bottom). Almost all features are either pharmacokinetic (1, 5, and 10) or textural in nature (2, 3, 6, 7, 8, and 9). Furthermore, although texture features show more change in successfully ablated tissue relative to the pharmacokinetic features, they also show large change in the residual disease.

Compared to the results of Viswanath et al.,⁶ we find that diffusion-weighted features seem of less importance. They compared the ablation zone to normal prostate tissue and found the diffusion-weighted feature to be most discriminative. In our case, comparing residual disease to successfully ablated tissue, diffusion-weighted features do not seem important. This indicates that, relative to normal tissue, there is a change in diffusion-weighted features; however, this change is similar in residual disease and successfully ablated tissue. This again shows that diffusion-weighted imaging might be less useful for detection of residual disease.

3.3 Objective 3: Combine Computer-Extracted Features with Feature Change to Better Discriminate Residual Disease from Successfully Ablated Tissue

For objective (3), we show that combining the computer extracted features with the relative feature differences, we improved detection of the residual disease, which is presented quantitatively in Table 3, column 2 and qualitatively in Fig. 7. For all patients, we can see that incorporating change in the feature values between pre- and post-LITT MRIs substantially

Table 3 Area under the curve on a voxel-by-voxel basis for detecting residual disease. The second column shows the effect of adding the differences between pre- and post-LITT MRIs for the 10 scoring features as extra features (Table 2).

Patient	Features	Features + feature differences
Patient 1	0.80	0.97
Patient 2	0.62	0.69
Patient 3	0.69	0.78

improves performance. For one patient, we were even able to achieve an AUC of 0.97, compared to 0.80 when using only post-LITT MRI features.

These results show that, using accurate registration of histopathology and the pre- and post-LITT MRIs, it is possible to identify features which might be useful in tracking treatment

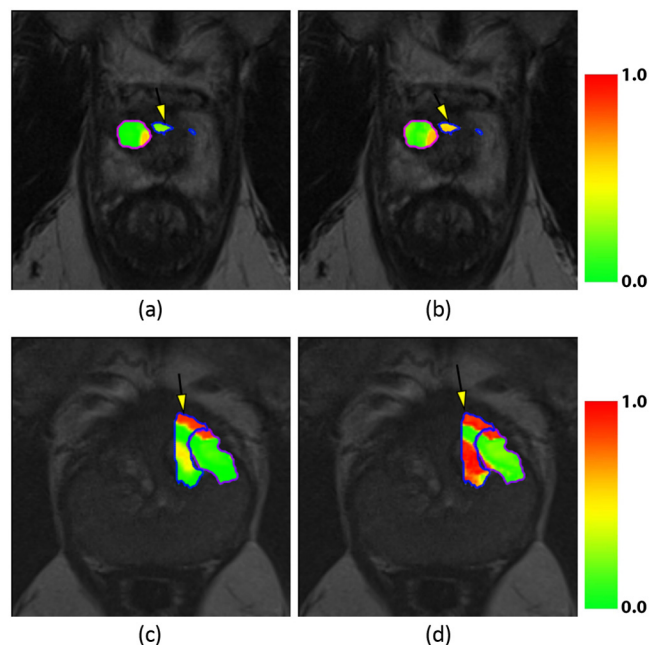


Fig. 7 Likelihood heat maps for the fuzzy C-means clustering separating treatment effects and residual disease. Patient 1 (a and b) and patient 3 (c and d) are shown. Figures (a and c) show the results obtained when only including post-LITT MRI feature, whereas figures (b and d) show the improvement obtained by incorporating the 10 highest scoring features (Table 2). Residual disease in blue, ablated area in purple. The residual disease area is also indicated with a yellow arrow.

success. Furthermore, in the future, we might be able to give quantitative guidelines for the treating physician to help him detect the presence of residual disease and predict patient outcome after successful ablation.

4 Concluding Remarks and Contributions

A unique clinical trial at the Radboud University Medical Center, in which four patients underwent a prostatectomy after LITT treatment, yielded *ex vivo* histopathologic specimens along with pre- and post-LITT MRIs. In this work, we used these data to address a unique set of questions: (1) are there imaging characteristics specific for residual disease and treatment effects? (2) Can we identify features which showed the most treatment-related change relative to residual disease? And (3) can we improve detection of residual disease by incorporating feature change in addition to post-LITT MRI features? By co-registering histology, pre- and post-LITT MRIs, we were able to build a methodological pipeline which allowed us to identify features which (1) differentially express between residual disease and treatment effects (AUC up to 0.80, Table 3). However, the results over all three patients showed that more information is needed to increase the accuracy in the detection of residual disease; for example, by incorporating feature change.

The main take-aways of this study are:

- The differences between residual disease and successfully ablated tissue cannot be fully characterized by taking just the post-LITT MRI into account.
- Different changes in features can be observed between pre- and post-LITT MRIs for residual disease and successfully ablated tissue.
- Incorporating feature changes as extra features discriminating residual disease and successfully ablated tissue results in an improved detection of residual disease.
- Diffusion-weighted imaging seems less important in assessing therapy effects compared to DCE or T2-weighted imaging.

Our study also has several limitations. The most important one is the lack of additional patient data. Currently, the initial results of the clinical trial are being investigated and will hopefully lead to an extended clinical trial. This will allow us to perform statistical tests to assess the significance of our results. Additionally, this will open up the opportunity to do a supervised classification of residual disease on the post-LITT MRI, which is now limited due to the substantial differences in treatment response in the three patients. As such, the results of this study should be viewed as preliminary. We do feel that the established methodology is a worthwhile path to better understanding of treatment-related changes in focal therapy of prostate cancer.

We assessed the stability of our results by performing the feature ranking several times in a leave-one-patient-out manner. Although the positions of features within the ranking changed during this experiment, the selected features themselves did not. As such, albeit the small dataset, results seem relatively stable.

Important methodological aspects of this work are the co-registration of histopathology and post-LITT MRI and the subsequent registration of the pre- and post-LITT MRIs. For the histopathology to MRI registration, it is difficult to assess the exact accuracy of the method in this limited dataset, but previous

reports in the literature using a similar methodology have reported errors of around 1.5 mm.^{10,23,24} Even if registration errors were two times larger, the registration error is still relatively small compared to the lesion sizes (around 10 mm). As such, we do not expect the histopathology to MRI registration to have a big impact on the obtained results, although a better registration methodology could allow for improved lesion characterization and might be mandatory in cases with small lesions. For example, improvements could be achieved by using 3-D registration, prostate molds, and *ex vivo* MRI of histopathologic specimens or the addition of synthetic fiducials.^{25,26}

For the pre- and post-LITT MRI registrations, one limitation of this study is the fact that we did not use biomechanical regularization to the ablated area in the case where elastic registration was applied. As such, it is assumed that this region has the same biomechanical properties as the rest of the prostate, which may not be accurate and could lead to registration errors. However, as the lesion is quite far from the endorectal coil, we expect compression to be limited at the area of ablation and the errors introduced due to neglecting changes in biomechanical properties to be small. This hypothesis is supported by the fact that registration of the ablated area to the pre-LITT MRI only resulted in a volume change of 4%. In future work, we intend to evaluate our data on a larger cohort and investigate the use of supervised classification over clustering.

Acknowledgments

Research reported in this publication was supported by the National Cancer Institute of the National Institutes of Health under Award Nos. R01CA136535-01, R01CA140772-01, and R21CA167811-01; the National Institute of Diabetes and Digestive and Kidney Diseases under Award No. R01DK098503-02, the DOD Prostate Cancer Synergistic Idea Development Award (PC120857); the QED award from the University City Science Center and Rutgers University, the Ohio Third Frontier Technology development Grant. The content is solely the responsibility of the authors and does not necessarily represent the official views of the National Institutes of Health.

References

1. J. Hegarty et al., "Radical prostatectomy versus watchful waiting for prostate cancer," *Cochrane Database Syst. Rev.* (11), CD006590 (2010).
2. A. B. Rosenkrantz et al., "Role of MRI in minimally invasive focal ablative therapy for prostate cancer," *AJR Am. J. Roentgenol.* **197**(1), W90–W96 (2011).
3. A. Oto et al., "MR imaging-guided focal laser ablation for prostate cancer: phase I trial," *Radiology* **267**, 932–940 (2013).
4. H. U. Ahmed et al., "Do low-grade and low-volume prostate cancers bear the hallmarks of malignancy?," *Lancet Oncol.* **13**, e509–e517 (2012).
5. H. R. Roberts et al., "Dynamic magnetic resonance control of interstitial laser photocoagulation therapy of colorectal hepatic metastases," *Lancet* **343**, 1221 (1994).
6. S. Viswanath et al., "Quantitative evaluation of treatment related changes on multi-parametric MRI after laser interstitial thermal therapy of prostate cancer," *Proc. SPIE* **8671**, 86711F (2013).
7. B. Pickett et al., "Use of MRI and spectroscopy in evaluation of external beam radiotherapy for prostate cancer," *Int. J. Radiat. Oncol. Biol. Phys.* **60**, 1047–1055 (2004).
8. I. Song et al., "Assessment of response to radiotherapy for prostate cancer: value of diffusion-weighted MRI at 3 T," *AJR Am. J. Roentgenol.* **194**, W477–W482 (2010).

9. U. Lindner et al., "Focal laser ablation for prostate cancer followed by radical prostatectomy: validation of focal therapy and imaging accuracy," *Eur. Urol.* **57**, 1111–1114 (2010).
10. J. Chappelow et al., "Elastic registration of multimodal prostate MRI and histology via multiattribute combined mutual information," *Med. Phys.* **38**, 2005–2018 (2011).
11. G. Litjens et al., "A pattern recognition approach to zonal segmentation of the prostate on MRI," *Lec. Notes Comput. Sci.* **7511**, 413–420 (2012).
12. S. E. Viswanath et al., "Central gland and peripheral zone prostate tumors have significantly different quantitative imaging signatures on 3 T endorectal, in vivo T2-weighted MR imagery," *J. Magn. Reson. Imaging* **36**, 213–224 (2012).
13. Q. Li, S. Sone, and K. Doi, "Selective enhancement filters for nodules, vessels, and airway walls in two- and three-dimensional CT scans," *Med. Phys.* **30**, 2040–2051 (2003).
14. P. C. Vos et al., "Automatic computer-aided detection of prostate cancer based on multiparametric magnetic resonance image analysis," *Phys. Med. Biol.* **57**, 1527–1542 (2012).
15. K. Kitajima et al., "Prostate cancer detection with 3 T MRI: Comparison of diffusion-weighted imaging and dynamic contrast-enhanced MRI in combination with T2-weighted imaging," *J. Magn. Reson. Imaging* **31**, 625–631 (2010).
16. J. O. Barentsz et al., "ESUR prostate MR guidelines 2012," *Eur. Radiol.* **22**, 746–757 (2012).
17. P. Tiwari, J. Kurhanewicz, and A. Madabhushi, "Multi-kernel graph embedding for detection, gleason grading of prostate cancer via MRI/MRS," *Med. Image Anal.* **17**, 219–235 (2013).
18. S. Klein et al., "Elastix: a toolbox for intensity-based medical image registration," *IEEE Trans. Med. Imaging* **29**, 196–205 (2010).
19. G. Litjens et al., "Automated computer-aided detection of prostate cancer in MR images: from a whole-organ to a zone-based approach," *Proc. SPIE* **8315**, 83150G (2012).
20. B. Li et al., "Establishing a normative atlas of the human lung: inter-subject warping and registration of volumetric CT images," *Acad. Radiol.* **10**, 255–265 (2003).
21. P. S. Tofts et al., "Estimating kinetic parameters from dynamic contrast-enhanced t(1)-weighted MRI of a diffusable tracer: standardized quantities and symbols," *J. Magn. Reson. Imaging* **10**, 223–232 (1999).
22. H. J. Huisman, M. R. Engelbrecht, and J. O. Barentsz, "Accurate estimation of pharmacokinetic contrast-enhanced dynamic MRI parameters of the prostate," *J. Magn. Reson. Imaging* **13**, 607–614 (2001).
23. Y. Zhan et al., "Registering histologic and MR images of prostate for image-based cancer detection," *Acad. Radiol.* **14**, 1367–1381 (2007).
24. M. Rusu et al., "Prostatome: a combined anatomical and disease based MRI atlas of the prostate," *Med. Phys.* **41**, 072301 (2014).
25. H. Trivedi et al., "Use of patient-specific MRI-based prostate mold for validation of multiparametric MRI in localization of prostate cancer," *Urology* **79**, 233–239 (2012).
26. E. Gibson et al., "Registration of prostate histology images to ex vivo MR images via strand-shaped fiducials," *J. Magn. Reson. Imaging* **36**, 1402–1412 (2012).

Biographies of the authors are not available.